

Simulation and Prediction of the Indian Ocean Dipole in the POAMA Seasonal Forecast Model

Mei Zhao¹

Harry H. Hendon

Centre for Australian Weather and Climate Research
A partnership between the Australian Bureau of Meteorology and
Commonwealth Scientific Industrial Research Organization
Melbourne, Australia

¹ Corresponding author: M. Zhao, CAWCR, Bureau of Meteorology, GPO Box 1289, Melbourne, 3001, Australia; email: m.zhao@bom.gov.au

Abstract

Predictive skill of the Indian Ocean Dipole (IOD) using the Bureau of Meteorology's POAMA seasonal forecast model is assessed in light of the model's ability to simulate the IOD. The analysis is based on a ten-member ensemble of nine-month forecasts that are initialized from observed ocean and atmosphere states once per month for the period 1982-2006. The observed IOD develops in late boreal spring, peaks in autumn and decays abruptly in winter, with about ½ of the variance of the IOD being associated with El Niño/Southern Oscillation (ENSO). The seasonal phase locking of the development of the IOD is well depicted in the POAMA forecasts but the IOD's structure is distorted and its amplitude weakens with increasing forecast lead time, while at the same time the IOD becomes spuriously over-dependent on ENSO. These deficiencies in the simulation of the IOD are attributed to inadequate horizontal resolution and development of biases in the mean state, which together affect depiction of important coupled dynamics for the IOD and of remote forcing by ENSO (which itself exhibits distortion of its spatial structure attributed to biases in the simulated mean state). Skilful prediction of the peak phase of the IOD in the September-November is limited to about 4-5 month lead time, with a rapid drop off in skill for forecasts initialized before June. Forecast skill for the IOD appears to be limited mainly by ability to predict development of SST anomalies in its eastern pole. Potential predictability estimates, assuming a perfect model, indicate great scope for improved prediction, although the IOD is much less predictable (potentially and in practice) than ENSO. However, the deficient depiction of the IOD at longer lead times means that estimates of potential predictability assuming a perfect model may be unreliable.

1. Introduction

Dynamical prediction of seasonal climate is founded on the ability to predict slow variations of anomalous boundary forcing, primarily associated with low frequency variations of tropical sea surface temperature (SST; e.g., Charney and Shukla 1981; Palmer and Anderson 1994; Goddard et al. 2001). Much of the predictable component of global seasonal climate variability can be attributed to teleconnections driven by anomalous convection that is forced by the tropical Pacific SST anomalies during El Niño/Southern Oscillation (ENSO; e.g., Brankovic et al. 1994; Stockdale et al. 1998). Thus, predictability of seasonal climate in many parts of the globe stems from and is limited by the predictability of the SST variations associated with ENSO itself. The current limit of predictability of SST variations associated with ENSO using dynamical coupled model systems is 2-3 seasons (e.g., Latif et al. 1998; Stockdale et al. 1998), though some recent studies suggest that certain ENSO episodes may be predictable more than 1 year in advance (Chen et al. 2004; Luo et al. 2008).

ENSO is not the only important source of low frequency climate variability that may be potentially predictable. For instance, low frequency variations of SST in the tropical Atlantic and Indian Oceans are the source of important climate anomalies throughout the globe (e.g., Nicholls 1989; Goddard and Graham 1999; Saji and Yamagata 2003; Kushnir et al. 2006). In the case of the Atlantic, contemporary dynamical forecast systems show little skill beyond 1 or 2 months in predicting tropical SST variations and are no better than persistence (e.g., Stockdale et al. 2006), apparently stemming from a combination of model error (especially bias in simulating the mean state), deficient ocean initial conditions, and the relatively weak role of (slow) subsurface variations for control of SST as compared to the Pacific. On the other hand, despite similar limitations from model error, deficient ocean initial conditions and chaotic atmospheric forcing, some success in predicting low frequency SST variations in the tropical Indian Ocean has recently been reported (e.g., Wajsowicz 2007; Luo et al. 2007)

Compared to the equatorial Pacific, predictability of low-frequency variations of SST in the Indian Ocean is expected to be more limited as a result of weaker coupling of the SST to subsurface variations, strong interactions with the Australian-Asian monsoon, and chaotic forcing by intraseasonal oscillations in both the atmosphere and ocean. Like the tropical Atlantic, ENSO is a major source of remote forcing of low frequency SST variability in the tropical Indian Ocean (Klein et al. 1999; Alexander et al. 2002; Shinoda et al. 2004a; Lau and Nath 2004; Saji et al. 2006). Hence, predictability of SST and climate variability in general in the tropical Indian Ocean stems from and is also limited, in part, by the ability to predict ENSO. But, it is now recognized that the Indian Ocean supports its own low frequency mode of coupled ocean-atmosphere variability, the Indian Ocean Dipole (IOD) or zonal mode (e.g., Saji et al. 1999; Webster et al. 1999), which plays a role in the Indian Ocean response to remote forcing from ENSO (e.g., Baquero-Bernal et al. 2002; Huang and Kinter 2002; Shinoda et al. 2004b; Zhong et al. 2005) but also acts on its own to generate low frequency climate variations (e.g., Fischer et al. 2005; Behera et al. 2006; Saji et al. 2006). Hence, the IOD may be a source of predictability beyond that of ENSO.

Recent estimates of predictability of the IOD (Wajsowicz 2004, 2005, 2007; Luo et al. 2007) suggest a current practical limit of about 1 season with a strong boreal spring prediction barrier stemming from the strong phase locking of the IOD to the seasonal cycle. Potential predictability estimates, which are based on a ‘perfect model’ assumption, suggest that the current practical limit is well below what might be achievable with improved initial conditions (e.g., Wajsowicz 2007). However, such estimates of potential predictability are highly model dependent. Furthermore, estimates of forecast skill are affected by mean-state drift and other model errors in addition to poor initial conditions. Realistic simulation of the mean state of the Indian Ocean that is relevant to the IOD (e.g., maintenance of the mean east-west gradients of thermocline depth and SST) is notoriously difficult (e.g., Fisher et al. 2005; Cai et al. 2005; Saji

et al. 2006). Biases in the mean state not only affect the realistic simulation of the coupled dynamics of the IOD, but also its relationship (independence) with ENSO (Wajsowicz 2004, 2007; Saji et al. 2006). The question thus arises as to the relationship between the realism of simulating the IOD in a coupled forecast model (including the mechanism of air-sea coupling, the spatial structure, the phase locking to the seasonal cycle and the dependence upon ENSO) and the skill of forecasting the IOD.

We will address this question by examining the prediction skill of the IOD using the Australian Bureau of Meteorology POAMA seasonal forecast model. By making use of an ensemble of forecasts, we will provide both estimates of actual predictive skill and of potential predictability of the IOD in a fashion similar to Wajsowicz (2007). We will explore impacts of biases in the mean state on the simulation and prediction of the IOD and we will address how such biases affect the dependence of the IOD on ENSO. We will relate loss of predictability at longer lead times to deleterious impacts of model drift on the forecast model's ability to simulate the IOD. Hence, while we find predictive skill of the IOD to be limited to about 1 season in the current version of the POAMA system, these results give some hope that model improvements in the representation of the mean state and coupled processes in the Indian Ocean of relevance to the IOD may lead to significant improvements in predictive skill of the IOD.

2. Model configuration, data, and index definition

2.1 POAMA model

For this study we use a 10-member ensemble of nine month hindcasts from POAMA (Predictive Ocean Atmosphere Model for Australia) version 1.5. POAMA is based on coupled ocean and atmosphere general circulation models (Alves et al., 2003). The atmospheric component of the coupled model is the Bureau of Meteorology unified atmospheric model (BAM) version 3.0d. BAM is a spectral transform model, which is run here with triangular

truncation 47 and 17 vertical levels. Some relevant model physics include a mass flux convection scheme with a CAPE tendency closure that supports a reasonable Madden-Julian Oscillation (e.g., Zhang et al. 2006), three active soil layers for temperature, and a simple bucket scheme for soil moisture that has a field capacity of 150mm (Manabe and Holloway 1975). The ocean model component is the Australia Community Ocean Model version 2 (ACOM2). It was developed from the Geophysical Fluid Dynamics Laboratory (GFDL) Modular Ocean Model (MOM version 2). The grid spacing is 2 degrees in the zonal direction. The meridional spacing is 0.5° within 8° of the equator, increasing gradually to 1.5° near the poles. There are 25 levels in the vertical, with 12 in the top 185 metres. The maximum depth is 5,000 metres. The level thicknesses range from 15 metres near the surface to almost 1,000 metres near the bottom. Technical details and some aspects of the performance of the model, including the depiction of the Indonesian throughflow, are provided in Schiller et al. (1997) and Schiller et al. (2002). The ocean and atmosphere models are coupled using the Ocean Atmosphere Sea Ice Soil (OASIS) coupling software (Valcke et al. 2000) with no flux correction applied. Surface ocean currents are taken into account for computation of the surface stress that is provided to the ocean model. Coupling occurs every 3 hours.

Ocean initial conditions for the hindcasts are produced by an ocean data assimilation scheme that is based on the optimum interpolation (OI) technique described by Smith et al. (1991). Only temperature observations are assimilated and only measurements in the top 500 m are used. The OI scheme is used to correct the ocean model background field every 3 days using a 3 day observation window. Corrections to currents are calculated by applying the geostrophic relation to the temperature corrections, similar to the method described by Burgers et al. (2002). Atmospheric initial conditions are provided by the Atmosphere-Land Initialization (ALI) scheme (Hudson and Alves 2007). ALI involves the creation of a new reanalysis dataset using the atmospheric model of POAMA, whereby the atmospheric model fields of velocity, temperature

and humidity are nudged toward reanalyses from ERA-40 (Uppala et al. 2005). This nudging process results in atmospheric and land surface fields that are in balance, while the resulting atmospheric fields are very similar to the ERA-40 reanalysis but are more in balance with the BAM 3.0d atmospheric model than would be if the ERA-40 fields were used directly as initial conditions. ALI operates by running an offline version of BAM forced by observed SST (Reynolds et al. 2002) for the period 1982-2006. Each 6 hours, the fields of velocity, temperature and humidity from the atmospheric model are compared to the verifying fields from ERA-40, and $\frac{1}{2}$ of the difference is added to the model fields. In this process, soil moisture and temperature is initialized indirectly via the nudged atmosphere, and the soil moisture and temperature evolve consistent with the atmospheric forcing.

An ensemble of 10 members of hindcasts for start times January 1982 through December 2006 was then generated from the observed ocean and atmosphere initial conditions valid for the 1st of each month. The ensemble was generated by perturbing the atmospheric initial conditions by successively picking the analysis from a 6 hour earlier period (i.e. the tenth member was initialized 2.5 days earlier than the first member). There was no perturbation applied to the ocean initial conditions. All forecasts were run for 9 months. We adopt the terminology that a lead time of 1 month means a forecast initialized on, for instance, 1 January that is valid for the month of January. Forecast anomalies are formed relative to the forecast model climatology, which is a function of start month and lead time. In this fashion, the mean bias from the forecasts is removed.

2.2 Climate indices

Forecasts will be assessed using indices of SST and zonal wind that are relevant to the IOD and ENSO. Following Saji et al. (1999), the Dipole Mode Index (DMI) is defined as the SST anomaly difference between the western pole (WIO, 50°-70°E, 10°S-10°N) and eastern pole (EIO, 90°-110°E, 10°S-0°) of the tropical Indian Ocean. The Niño3.4 index is defined as SST

anomaly averaged in the equatorial Pacific (170°-120°W, 5°S-5°N). The surface zonal wind index at 10-m height (U10) anomaly in the central equatorial Indian Ocean (70°-90°E, 5°S-5°N) is defined as in Luo et al. (2007). The tropical Indian Ocean (IO) region is defined as: 20°S-30°N, 40°E-110°E.

2.3 Verification data

For SST, we verify against the NOAA Optimum Interpolation (OI) SST V2 data (Reynolds et al. 2002; hereafter, Reynolds data). These data are also used to drive the atmospheric component of POAMA in order to generate an AMIP-style simulation. We will compare some of the fully coupled hindcast results with AMIP-style results in order to investigate the impact of biases in the atmospheric component model for generating biases in the coupled model. Winds are verified against NCEP Reanalysis-1 monthly data (Kalnay et al. 1996). The depth of 20 °C isotherm (d20) and the heat content (mean temperature) in the upper 300 m (HC) are verified against the data from the POAMA ocean assimilation that is used to provide initial conditions (described above). For precipitation we compare with CMAP monthly precipitation (Xie and Arkin 1997), which is developed from 5 satellite estimates and blended with the NCEP/NCAR reanalysis. Anomalies are formed by subtracting the climatological seasonal cycle over 1982-2006 period.

3. Simulated behavior of IOD

3.1 Mean state bias and variability

We begin by examining some aspects of the mean state predicted by POAMA that are relevant to the IOD. Following Fischer et al. (2005) and Luo et al. (2007), we present in Fig. 1a-c ensemble mean climatologies, as a function of lead time, for SST, U10, and d20 along the equator in the Indian Ocean (2°S-2°N). POAMA is non-flux corrected so the mean state drifts, and the drift increases with lead time. Even for lead time one month, the SST across much of the equatorial Indian Ocean has already cooled ~0.5 K (Fig. 1a). By 9 month lead time the Indian

Ocean has cooled ~ 2 K, which is symptomatic of cooling throughout the Tropics in this model. This tropical-wide cold bias appears to stem from a surface shortwave radiation bias as a result of too much tropical low cloud. The cooling across the Indian Ocean is greater in the east than in the west, which results in a reduction of the west-east temperature gradient along the equator (observed is ~ 2 K and simulated at 9 month lead time is ~ 1 K). Associated with the weakened west-east temperature gradient, the surface zonal wind (Fig. 1b), which is observed to be westerly in the central and east Indian Ocean, weakens with increased lead time. At short lead time (1 month) the distribution of westerlies is fairly realistic, but by lead time 9 month surface westerlies have completely disappeared in the central part of the basin. Associated with weakened westerlies, the equatorial thermocline erroneously shoals to the east with increased lead time (Fig. 1c). While the thermocline is initially slightly too deep in the eastern Indian, by 9 month lead time it has shoaled some 10-15 m.

The implication of these biases in the mean state for simulation and prediction of coupled variability in the Indian Ocean is assessed by examining the variability (standard deviation) of SST, zonal wind and thermocline depth along the equator (Figs. 1d-f). Here we compute the standard deviation for each month using each ensemble member, and then average the standard deviation over all 10 ensemble members. In this fashion, the contribution of “noise” to the variability in each member is retained and comparison with the single observed realization is straightforward. Despite the large (and increasing with lead time) cold bias in the mean state, SST variability is simulated to be only marginally reduced compared to the observed variability. There appears to be a significant reduction in SST variability at short lead time (peaking at lead time 3 months) in the far eastern Indian Ocean, which is a key region for the IOD, but variability there recovers at longer lead time. However, the maximum observed variability right at the eastern boundary, associated with upwelling on the Sumatra Coast, is absent at all lead times. We speculate that this reflects inadequate horizontal resolution in both the ocean and atmospheric

models (discussed further below). Overall, however, SST variability is relatively successfully simulated despite the large cold bias in the mean state.

Surface zonal wind variability is observed to be maximum in the central Indian Ocean (Fig. 1e), which presumably reflects fluctuations of the mean west-east SST gradient as a result of the IOD (e.g. Saji et al. 1999), of ENSO (e.g., Klein et al. 1999), and of other processes such as air-sea coupling in the seas of western Indonesia (Hendon 2003). However, even at short lead time when the SST bias is small, the zonal wind variance is under-represented in the model (50°E-85°E), although a local maximum in the central part of the basin is realistically depicted. Again, there is some recovery of the zonal wind variance at longer lead times, consistent with the recovery of SST variance in the eastern Indian Ocean (Fig. 1d). The reduction of zonal wind variance in the central Indian Ocean, even at short lead time, suggests problems stemming from the atmospheric model. This is confirmed by using the AMIP-style integration of the atmospheric model, where by the atmospheric model is forced with observed SST for the same period 1982-2006 (dot-dash line in Fig. 1e). Even with the observed SST specified, the atmospheric model can not reproduce the observed level of zonal wind variability in the central Indian Ocean. This may also stem from inadequate horizontal resolution, whereby the coarse grid of the atmospheric model (roughly 2.5 degrees longitude) is unable to fully resolve and respond to important, but zonally narrow, SST variations along the Java-Sumatra Coasts. Interestingly, the reduction in zonal wind variance is not reflected in a similar reduction (except at lead time 3 months) in thermocline variance in the eastern part of the basin (Fig. 1f), where IOD influences are important.

Seasonal variations of the mean state of the Indian Ocean play a primary role for producing the seasonal phase-locking of the IOD (e.g., Saji et al. 2006). We found that, despite the strong bias in the annual mean SST, the seasonal cycle of SST in the east and west equatorial Indian Ocean are realistically simulated (not shown). However, the seasonal cycle of the standard

deviation of SST in the eastern Indian Ocean (not shown), which is observed to have a strong maximum in SON and another weaker maximum in Feb-March, is under represented in SON by 10-20% (greatest reduction is at lead time 3 months). This suggests that the IOD is simulated to be too weak in the model forecasts, which is confirmed by examining the annual cycle of the standard deviation of the DMI (Fig. 2a). The observed DMI peaks strongly in SON and is a minimum in Jan-Apr. The simulated DMI in the forecast model exhibits a realistic seasonal variation but its maximum in SON is too weak and it does not drop off as quickly in Dec-Jan as observed. As for the zonal wind variance in the central Indian Ocean (Fig. 1 e) and SST variance in the eastern Indian Ocean (Fig. 1d), the DMI initially weakens through lead time 3 months and then recovers somewhat at longer lead time. Our interpretation of the reduced amplitude of the simulated DMI is that the forecast model is not able to simulate the growth phase of the IOD in the June-October period. This deficiency probably stems from errors in the coupled dynamics of the Indian Ocean, but we can not discount errors in the representation of the remote forcing from ENSO. Inspection of the annual variation of the amplitude of the Niño3.4 index indicates realistic amplitude and seasonal variation (peak in Nov-Jan; Fig. 2b), suggesting that any errors in remote forcing from ENSO do not stem from an erroneous depiction of the phase locking to the seasonal cycle of El Niño development (e.g. Zhong et al. 2005).

3.2 Characteristics of simulated IOD

We now look in more detail at the characteristics of the simulated IOD by the forecast model. The IOD is identified as the leading Empirical Orthogonal Function (EOF) of SST in the tropical Indian Ocean region for the September-November (SON) season (e.g., Saji et al. 1999). We concentrate on the SON season because this is when the IOD has largest amplitude (Fig. 2). The eigenvector (spatial pattern) of EOF1, superposed on the standard deviation of SST, is shown in Fig. 3 for observations and for the model forecasts at lead times 1-, 3-, 6-, and 9-month. For the analysis of the model output, we created SON means by averaging forecasts with

the same lead time (e.g., for lead time 1 we average the September forecasts from 1 September starts with the October forecasts from 1 October starts and with the November forecasts from the 1 November starts). In this fashion, the impact of model drift is equally expressed in all three months. We then average over all ten ensemble members and compute the EOFs.

Observed EOF1 (Fig. 3a) exhibits a zonal dipole pattern in SST; the eastern pole is concentrated just south of the equator and is anchored on the Java-Sumatra coast and the western pole has maxima off of the equator in the western Indian Ocean (e.g., Saji et al. 1999). The regions of maximum loading of the eigenvector coincide well with the maxima in standard deviation, indicating the dominance of the IOD for basin-wide SST fluctuations in the SON season (EOF1 accounts for 35% of the observed variance for SON). At all lead times, the leading EOF from the forecasts appears as a dipole, although the SST anomaly in the eastern pole weakens and distorts especially off of the Java-Sumatra coast with increasing lead time. This is quantified by the spatial anomaly correlation between EOF1 from observations and forecasts (Table 1), which is over 0.9 at lead time 1 month but then gradually drops to 0.55 by lead time 7 month, and thereafter recovers slightly. Together with a decrease in the realism of the pattern of EOF1 with increasing lead time, the explained variance by EOF1 spuriously increases with increasing lead time, increasing from 43% at lead time 1 month to 58% at lead time 9 month (recall that the use of ensemble mean forecast data necessarily implies that the leading EOF will account for more variance than observed). We will show below that this increasing dominance of EOF1 also coincides with a spurious increase in the dependence of EOF1 on El Niño with increasing lead time.

The principal component (loading time series) of EOF1 (PC1) from observations is shown in Fig. 3b. Positive dipole events are identified in 1982, 1987, 1994, 1997, 2002, and 2006, which are also El Niño years (1994 is considered by some not to be an El Niño year). For the record used here (1982-2006), the correlation between observed PC1 and the observed Niño3.4

index for SON is 0.68 (Table 2), which emphasises the strong relationship between most dipole events and El Niño. However, the correlation is generally weaker when longer records are considered (e.g., Saji et al. 2006). The correlation between PC1 and the Niño3.4 index from the forecasts, while realistic at short lead time, increases with increasing lead time, peaking at 0.86 at lead time 6 months (Table 2). It thereafter drops back to a realistic value of 0.68 at lead time 9 months. Our interpretation of this behavior is that the air-sea coupled feedbacks in the tropical Indian Ocean that give rise to the IOD weaken with increasing lead time (up to lead 6-7 months) and thus the simulated IOD becomes more dependent on El Niño for excitation.

In order to see more clearly the depiction of the IOD and its relationship with ENSO in the forecast model, we develop regressions against PC1 for SST and HC (Fig. 4) and surface winds (vector), and precipitation (Fig. 5) from observations and from forecasts at lead times 1, 3, 6, and 9 months. The observed IOD is understood to result from a coupled feedback between winds, SST and rainfall (Figs. 4a,f and 5a): negative SST anomaly and suppressed rainfall south of the equator along the Sumatra-Java coast drive an anticyclonic circulation anomaly, with the resultant south-easterlies along the Java-Sumatra coast locally acting to enhance coastal upwelling and latent heat flux and further cooling the SST. Easterlies anomalies in the central part of the basin excite an upwelling oceanic Kelvin wave response that further acts to elevate the thermocline in the east and promote cooling of the SST in the east. The equatorial easterlies also excite downwelling oceanic Rossby waves, which act to warm the SST to the west, especially south of the equator where the mean thermocline ridges in response to mean equatorial westerlies (e.g. Xie et al. 2002). Warmer SSTs in the western Indian Ocean further promote enhanced rainfall in the west and suppressed rainfall in the east, which enhances the easterly anomalies in the central part of the basin. The regression based on observed fields also highlights that the IOD is often associated with El Niño conditions in the Pacific (positive SST and rainfall anomalies in the central-eastern equatorial Pacific, suppressed thermocline in the east equatorial

Pacific and elevated thermocline off of the equator in the west, together with westerly anomalies in the central Pacific). The IOD is also associated with elevated thermocline on the west coast of Australia (Fig. 4f), but this stems from El Niño in the Pacific (i.e. the “oceanic teleconnection”, Meyers 1996) and not directly from wind forcing by the IOD in the Indian Ocean.

At short lead times (1-3 months), the coupled dynamics of the IOD appear well represented in the forecast model (Figs. 4 b,c,g,h and 5 b,c). The weakened and distorted depiction of the IOD at longer lead times is evidenced by a zonally-contracted negative SST anomaly in the eastern pole, westward displaced wind and rainfall anomalies away from the Java-Sumatra Coast (e.g., the west-east dipole mode becomes north-south dipole mode), and much weaker thermocline anomalies that are indicative of weakened coupling with the subsurface. Biases in the structure of El Niño are also evident (westward displacement of the SST and rainfall anomalies in the equatorial Pacific). Hence, the overall impression is that the coupled dynamics of the IOD are not well represented at longer lead time. Rather, the model’s IOD at longer lead times appears to primarily stem from remote forcing from the Pacific (e.g. Shinoda et al. 2004a) associated with a spuriously westward shifted El Niño mode.

4. Forecast skill and potential predictability of the IOD

Forecast skill is measured using temporal anomaly correlation coefficient (ACC), which emphasizes phase errors, and the root mean square error normalized by the standard deviation of the verification (NRMSE), which emphasizes errors in magnitude. Calculation of these quantities is standard (e.g., Wilks 1995) and uses anomaly data (observed or hindcast climatology removed). An overall view of forecast skill of SST is given by the temporal ACC of ensemble mean SST, using all start months (Fig. 6). Skill, taken here to be an ACC greater than 0.6 (e.g., Hollingsworth et al. 1980), is exhibited in the central equatorial Pacific to at least lead time 9 months, which is associated with ENSO. Skill drops off much quicker in the Indian Ocean, with

only limited regions of correlation greater than 0.6 in the western Indian Ocean by lead time 3 months. Even after just one month, the correlation in the Indian Ocean is mostly less than 0.8 while it is greater than 0.9 in the equatorial central and eastern Pacific.

Specifically focusing on the IOD and ENSO, we show in Fig. 7 the temporal ACC and NRMSE for the DMI, the eastern (EIO) and western (WIO) poles separately, and the Niño3.4 index. We also include the ACC and NRMSE for a persistence forecast. Additionally, the standard deviation of the indices from the forecasts, normalized by the observed standard deviation (NSTD), is displayed. The measures of forecast skill in Fig. 7 are based on data from all start months, so the assessment of skill based on the DMI does not accurately reflect skill of predicting the IOD because the IOD is not well defined for the December-April portion of the year. This issue will be addressed below when we examine forecast skill as a function of start month. Nonetheless, the ACC and NRMSE for POAMA forecasts using all start months beats persistence at all lead times. For the Niño3.4 index, the ACC remains above 0.6 (Fig. 7d), and the NRMSE remains below 1 while the NSTD remains near 1 (Fig. 7h) to at least lead time 9 months. In contrast, the ACC for the DMI drops below 0.6 after only lead time 3 months (Fig. 7a). The NRSME for the DMI does remain below 1 (i.e., indicative of skill) until 5 month lead time (Fig. 7e), but this is an optimistic view of the error because the forecast DMI is losing amplitude. Again, this loss of amplitude of the DMI appears to stem from a loss of amplitude in SST in the eastern pole of the IOD (Fig. 7f), while the amplitude in the western pole is realistically maintained (Fig. 7g).

A better indication of forecast skill of the IOD is gained by assessing the ACC as a function of start month and lead time (Fig. 8a). Again we include the ACC computed for a persistence forecast (Fig. 8e). In Fig. 8, the sloping dotted lines are indicative of constant verification month but with increasing forecast lead time. Skill for the DMI (Fig. 8a) is clearly seen to be peaked for forecasts that verify in September-December, which is when the IOD is well defined. The

highest skill is for October-November verifications, with skill ($ACC > 0.6$) extending to ~5 month lead time. From the point of view of start time, skilful forecast of the IOD are only achievable for start months after May. That is, there is a boreal spring “barrier”, but this is partly accounted for by the fact that the IOD is not well defined prior to June. Persistence (Fig. 8e) is strongest for August-September verifications and is also only skilful for start months after May. Hence, the dynamical forecasts offer the greatest improvement over persistence for forecast verifying in October-December, which is when the IOD tends to peak and begins to decay. On the other hand, the dynamical model is unable to beat persistence for forecasts starting in April-May.

Forecast skill in the east pole of the IOD (Figs. 8 b) also peaks for September-November as for the DMI, but it is also high for February-April starts out to 3 month lead time. A recovery of skill for August-November starts at lead times beyond 5 months (forecasts verifying in February-April) is also seen, which coincides with a change in sign of persistence. This previously has been explained as a reflection of the delayed response to El Niño (e.g., Wajsowicz 2007), when the entire Indian Ocean tends to warm after the peak of El Niño. For the western Indian Ocean the greatest skill is for forecasts verifying in February-March, which is also thought to stem from the basin-wide warming in response to El Niño. In contrast to the Indian Ocean indices, skill ($ACC > 0.6$) for the Niño3.4 index (Fig. 8d) extends to beyond nine month lead time for all start months and is strongest for November-February verifications. As for the DMI, forecast skill for Niño3.4 increases for start months after May, however loss of forecast skill across this “spring barrier” is much less pronounced for Niño3.4 than for the DMI. Furthermore, the dynamical forecasts provide the biggest improvement over persistence for boreal spring starts.

By making use of the ten member ensemble, an estimate of potential predictability, assuming a “perfect model”, can be provided. We use the method of analysis of variance (e.g, Rowell et al. 1995), whereby the variance of the ensemble mean is compared to the total variance of the ensemble (ensemble mean plus variance of each member about the mean). The resulting

estimates of potential are nearly identical to those derived from the method used by Wasjowicz (2007), whereby successive members of the ensemble are taken as truth and scored against the ensemble mean of the remaining members. The method of analysis of variance (Rowell et al. 1995) assumes that the predictable fraction of the total variance of the ensemble, $Pred_{var}$, is given by

$$Pred_{var} = \frac{Var_{ensm}^*}{(Var_{ensm}^* + Var_{sprd})},$$

where $Var_{ensm}^* = Var_{ensm} - \frac{1}{N}Var_{sprd}$ is a non-biased estimate of the variance of the ensemble mean. Here $N=10$ members. The ensemble mean variance is computed over the 25 years of forecasts and the variance of the ensemble spread Var_{sprd} is computed using the deviation of each of the ten members about the ensemble mean for all 25 years.

The estimates of potential predictability are shown in Fig. 9. Comparison with actual skill (Fig. 8) indicates enormous scope for improved prediction. For example, skill for the forecasts of DMI that verify in October should be extendable by 3-4 additional months. The caveat of these estimates is, of course, that low spread (i.e. high skill) may stem from a biased ensemble as a result of forecast errors, including errors in initial conditions and in the model (e.g. Wasjowicz 2007). However, regions of actual high skill for the forecasts of DMI and Niño3.4 (Fig. 8) coincide with regions of low spread (high potential predictability), thus giving some confidence in the realism of the model.

Finally, performance of the forecast system is demonstrated for the major IOD events in 1994, 1997, and 2006. In Fig. 10, we plot the observed SST anomaly and the ensemble mean forecasts from the 1st of January, May, July, September and November for the DMI, EIO and WIO SSTA as well as Niño3.4 index. The thick solid black curve is the observation for each case. As anticipated from the above analysis of forecast skill, the demise of the IOD events after about October is well predicted 1-2 seasons in advance, but the magnitude of all three IOD

events is under-predicted. There is some indication of growth of the IOD (and cold anomaly in the eastern Indian Ocean) for the 1997 event from as early as July initial conditions and for the 2006 event from as early as January initial conditions. But, no forecast picks up any growth for the 1994 event. Song et al. (2008) suggested that IOD events are more predictable if they occur along with El Niño. This seems to hold true for the forecasts here as the 1994 IOD was accompanied by a very weak El Niño event that started late in the seasonal cycle (i.e., after about August). On the other hand, the 1997 and 2006 IOD events were accompanied by El Niño events that began earlier in the seasonal cycle (before July). However, only the 1997 El Niño event was predicted before July.

5. Discussion and conclusions

Predictive skill of the IOD using the Bureau of Meteorology's POAMA seasonal forecast model was assessed in light of the model's ability to simulate the IOD. The analysis was based on a ten-member ensemble of nine-month forecasts that were initialized from observed ocean and atmosphere states once per month for the period 1982-2006. The observed IOD develops in late boreal spring, peaks in autumn and decays abruptly in winter, with about $\frac{1}{2}$ of the variance of the IOD being associated with ENSO. This seasonal phase locking of the development of the IOD is well depicted in the POAMA forecasts but the IOD's structure is distorted and its amplitude weakens with increasing forecast lead time. These deficiencies in the simulation of the IOD are attributed to inadequate horizontal resolution and development of biases in the mean state, which together affect depiction of the important coupled dynamics for the IOD. The relatively coarse horizontal grid of both the atmosphere and ocean model components of POAMA means that coastal upwelling along the Java-Sumatra coasts, which is a key contributor to the development of the IOD, is underrepresented. At longer lead time, the IOD is also simulated to become spuriously overly-dependent on ENSO. This appears to stem partly from

the biases in the Pacific ENSO mode (i.e., the westward extension of the ENSO related SST anomalies in the Pacific) as a result of the biases in the mean state of the Pacific cold tongue, thus causing the ENSO teleconnection into the Indian Ocean region to strengthen and shift westward at longer lead time. This biased ENSO teleconnection then acts in conjunction with the weakened depiction of the coupled dynamics of the IOD at longer lead time to result in an IOD that is too dependent on ENSO. However, the IOD is simulated to recover some amplitude and regain some independence from ENSO at the longest lead time (9-month), which we ascribe to the easterly bias of the mean surface zonal wind in the Indian Ocean basin that leads to an overly-shallow thermocline in the eastern equatorial Indian Ocean, hence promoting spuriously enhanced dynamical coupling via a Bjerknes feedback.

In light of these biases in the mean state and biases in depiction of the IOD at longer lead time, skilful prediction of the IOD is found to be confined to forecasts that verify in September-November and that are initialized after June. Skill drops off rapidly for forecasts initialized before June. Forecast skill for the IOD appears to be primarily limited by the ability to predict SST variations in its eastern pole, as forecast skill in the western pole is comparable to forecast skill of ENSO in the Pacific (i.e., skill in the western pole extends beyond 9 month lead time for forecasts initiated in the June-January period). These estimates of skill for prediction of IOD are comparable to other forecast systems based on fully coupled, non-flux corrected global climate models (e.g., Wajsowicz 2007). Recent work by Luo et al. (2007), using a coupled model system with little climate drift, suggests skilful prediction of the IOD for longer lead times (one or two seasons), but the use of 5 month mean data in their study makes direct comparison with the monthly data used here difficult. Nonetheless, a consistent message from this and other studies is that prediction of the IOD is limited to lead times much shorter than ENSO, reflecting both the more limited lifetime of the IOD as compared to ENSO and the overall lower level of predictability in the equatorial Indian Ocean than in the equatorial Pacific.

Potential predictability estimates, assuming a perfect model, do indicate great scope for improved prediction of the IOD. For the POAMA system, skilful prediction of the development and decay of the IOD is suggested out to 6 months and beyond. Hence, improved initial conditions in the Indian Ocean and elsewhere could indeed result in drastically improved prediction of the IOD. A major caveat of such an estimate of potential predictability is, of course, that it might be overly optimistic due to systematic error in the model whereby the forecasts have little spread but are all systematically wrong. The fact that the greatest actual skill coincides with the smallest spread (i.e. for forecasts of the IOD that verify in September-November beginning after June), does give us some hope that the model is behaving realistically. Nonetheless, further studies with other modelling systems are required as are additional studies that assess the impact of improved or degraded initial conditions in the Indian Ocean for forecast skill of the IOD. Furthermore, a reassessment of forecast skill is required in POAMA after the horizontal resolution of the component models is improved so as to better represent IOD physics and after major systematic errors in the mean state are alleviated. This work is ongoing and will be reported elsewhere.

Acknowledgments

We would like to thank our colleagues G. Liu and G. Wang for assistance in acquiring and working with the POAMA hindcasts and E. Lim and O. Alves for helpful discussion on aspects of the analysis. Support for this study was provided by the Western Australian Marine Science Institution. .

References

- Alexander, MA, Blade I, Newman M, Lazante JR, Lau NC, and Scott JD. 2002. The atmospheric bridge: The influence of ENSO teleconnections on air-sea interaction over the global oceans. *J. Climate* **15**: 2205-2231.
- Alves, O, Wang G, Zhong A, Smith N, Tseitkin F, Warren G, Schiller A, Godfrey S and Meyers G. 2003. POAMA: Bureau of Meteorology operational coupled model seasonal forecast system. Proc. National Drought Forum, Brisbane, Apr 2003, pp. 49-56. Available from DPI Publications, Department of Primary Industries, GPO Box 46, Brisbane, Qld 4001, Australia.
- Baquero-Bernal, A, Latif M, and Legutke S. 2002. On dipolelike variability of sea surface temperature in the tropical Indian Ocean. *J. Climate* **15**: 1358–1368.
- Behera, S K, Luo J J, Masson S, Rao S A, Sakuma H, and Yamagata T. 2006. A CGCM study on the interaction between IOD and ENSO. *J. Climate* **19**:1688-1705.
- Brankovic, C, and Palmer TN, and Ferranti L. 1994. Predictability of seasonal atmospheric variations. *J. Climate* **7**: 217–237.
- Burgers, G, Balmaseda MA, Vossepoel FC, Oldenborgh G, Leeuwen P. 2002. Balanced Ocean-Data Assimilation near the Equator. *J. Phy. Oceanography* **32**: 2509–2519.
- Cai, W, Hendon HH, and Meyers G. 2005. Indian Ocean dipolelike variability in the CSIRO Mark3 climate model. *J. Climate* **18**: 1449-1468.
- Chen, D, Can MA e, Kaplan A, Zebiak SE, and Huang D. 2004. Predictability of El Niño over the past 148 years. *Nature* **428**: 733-736.
- Charney, JG and Shukla J. 1981. Predictability of monsoons. *Monsoon Dynamics*, Editors: Sir James Lighthill and R. P. Pearce, Cambridge University Press, pp. 99- 109.

- Fischer AS, Terray P, Guilyardi E, Gualdi S, and Delecluse P. 2005. Two independent triggers for the Indian Ocean Dipole/Zonal Mode in a coupled GCM. *J. Climate* **18**: 3428-3349.
- Goddard, L, and Graham NE. 1999. The importance of the Indian Ocean for simulating rainfall anomalies over eastern and southern Africa. *J. Geophys. Res.* **104**: 19099-19116.
- Goddard, L, Mason SJ, Zebiak SE, Ropelewski CF, Basher R, and Cane MA. 2001. Current approaches to seasonal-to-interannual climate predictions. *Int. J. Climatol.* **21**: 1111-1152.
- Hendon, HH. 2003. Indonesian rainfall variability: Impacts of ENSO and local air-sea interaction. *J. Climate* **16**: 1775-1790.
- Hollingsworth, A, Arpe K, Tiedtke M, Capaldo M, and Savijaervi H. 1980. The performance of a medium range forecast model in winter—Impact of physical parameterizations. *Mon. Wea. Rev.* **108**: 1736–1773.
- Huang, B, and Kinter III JL. 2002. Interannual variability in the tropical Indian Ocean. *J. Geophys. Res.* **107**: 3199, doi:10.1029/2001JC001278.
- Hudson, D, and Alves O. 2007. The impact of land-atmosphere initialisation on dynamical seasonal prediction. CAWCR Research Report No.133, Bur. Met., Melbourne, Australia, 4pp.
- Kalnay E, Kanamitsu M, Kistler R, Collins W, Deaven D, Gandin L, Iredell M, Saha S, White G, Woollen J, Zhu Y, Leetmaa A, Reynolds B, Chelliah M, Ebisuzaki W, Higgins W, Janowiak J, Mo KC, Ropelewski C, Wang J, Jenne R, and Joseph D. 1996. The NCEP/NCAR 40-year reanalysis project. *Bull. Amer. Meteor. Soc.* **77**: 437-470.
- Klein, SA, Soden BJ, and Lau NC. 1999. Remote sea surface temperature variations during ENSO: Evidence for a tropical atmospheric bridge. *J. Climate* **12**: 917-932.
- Kushnir, Y, Robinson WA, Chang P, and Robertson AW. 2006. The physical basis for predicting Atlantic sector seasonal-to-interannual climate variability. *J. Climate* **19**: 5949-5970.

- Latif, M, Anderson D, Barnett T, Cane M, Kleeman R, Leetmaa A, O'Brien J, Rosati A, and Scheider E. 1998. A review of the predictability and prediction of ENSO. *J. Geophys. Res.* **103**: 14375-14393.
- Lau, NC, and Nath MJ. 2004. Coupled GCM simulation of atmosphere-ocean variability associated with the zonally asymmetric SST changes in the tropical Indian Ocean. *J. Climate* **17**: 245-265.
- Luo, JJ, Masson S, Behera S, and Yamagata T. 2007. Experimental forecasts of the Indian Ocean dipole using a coupled OAGCM. *J. Climate* **20**: 2178-2190.
- Luo, JJ, Mason S, Behera SK, and Yamagata T. 2008. Extended ENSO prediction using a fully coupled ocean-atmosphere model. *J. Climate* **21**: 84-93.
- Manabe, S, and Holloway, Jr JL. 1975. The seasonal variation of the hydrologic cycle as simulated by a global model of the atmosphere. *J. Geophys. Res.* **80**: 1617-1649.
- Meyers, G 1996. Variation of Indonesian throughflow and the El Niño-Southern Oscillation. *J. Geophys. Res.* **101**: 12255-12263.
- Nicholls, N 1989. Sea surface temperatures and Australian winter rainfall. *J. Climate* **2**: 965-973.
- Palmer, T and Anderson DLT. 1994. Prospects for seasonal forecasting – A review paper. *Quart. J. Roy. Meteor. Soc.* **120**: 755-793.
- Reynolds, RW, Rayner NA, Smith TM, Stokes DC, and Wang W. 2002. An Improved In Situ and Satellite SST Analysis for Climate. *J. Climate* **15**: 1609-1625.
- Rowell, DP, Folland CK, Maskell K, and Ward MN. 1995. Variability of summer rainfall over tropical North Africa (1906–92): Observations and modelling. *Quart. J. Roy. Meteor. Soc.* **121**: 669–704.
- Saji, NH, Goswami BN, Vinayachandran PN, and Yamagata T. 1999. A dipole mode in the tropical Indian Ocean. *Nature* **401**: 360-363.

- Saji, NH and Yamagata T. 2003. Possible impacts of Indian Ocean Dipole mode events on global climate. *Climate Res.* **25**: 151-169.
- Saji, NH, Xie SP, and Yamagata T. 2006. Tropical Indian Ocean variability in the IPCC twentieth-century climate simulations. *J. Climate* **19**: 4397-4417.
- Schiller, A, Godfrey JS, McIntosh P and Meyers G. 1997. A global ocean general circulation model climate variability studies. CSIRO Marine Research Report No.227, 60 pp.
- Schiller, A, Godfrey JS, McIntosh PC, Meyers G, Smith NR, Alves O, Wang G and Fiedler R. 2002. A New Version of the Australian Community Ocean Model for Seasonal Climate Prediction. CSIRO Marine Research Report No.240.
- Shinoda, T, Alexander MA, Hendon HH. 2004a. Remote response of the Indian Ocean to interannual SST variations in the tropical Pacific. *J. Climate* **17**: 362-372.
- Shinoda, T, Hendon HH, Alexander MA. 2004b. Surface and subsurface dipole variability in the Indian Ocean and its relation to ENSO. *Deep Sea Res.* **51**: 619-635.
- Smith, NR, Blomley JE and Meyers G. 1991. A univariate statistical interpolation scheme for subsurface thermal analyses in the tropical oceans. *Prog. Oceanogr.* **28**: 219-256.
- Song, Q, Vecchi GA, and Rosati AJ. 2008. Predictability of the Indian Ocean surface temperature anomalies in the GFDL coupled model. *Geophys. Res. Letters.* **35**: L02701, doi:10.1029/2007GL031966.
- Stockdale, TN, Anderson DLT, Alves JOS, and Balmaseda MA. 1998. Global seasonal rainfall forecasts using a coupled ocean-atmosphere model. *Nature* **392**: 370-373.
- Stockdale, TN, Balmaseda MA, and Vidard A. 2006. Tropical Atlantic SST prediction with coupled ocean-atmosphere GCMS. *J. Climate* **19**: 6047-6061.
- Uppala, SM, , Kallberg PW, Simmons AJ, Andrae U, Da Costa Bechtold V, Fiorino M, Gibson JK, Haseler J, Hernandez A, Kelly GA. 2005. The ERA-40 re-analysis. *Quart. J. Roy. Meteor. Soc.* **131(612)**: 2961-3012.

- Valcke, S, Terray L and Piacentini A. 2000. OASIS 2.4 Ocean Atmospheric Sea Ice Soil users guide, Version 2.4. CERFACS Tech. Rep, CERFACS TR/CMGC/00-10, 85pp.
- Wajsowicz, RC. 2004. Climate variability over the tropical Indian Ocean sector in the NSIPP seasonal forecast system. *J. Climate* **17**: 4783-4804.
- Wajsowicz, RC. 2005. Potential predictability of tropical Indian Ocean SST anomalies. *Geophysical Res. Lett.* **32**: L24702, doi:10.1029/2005GL024169.
- Wajsowicz, RC. 2007. Seasonal-to-interannual forecasting of tropical Indian Ocean sea surface temperature anomalies: Potential predictability and barriers. *J. Climate* **20**: 3320-3343.
- Webster, PJ, Moore AM, Loschnigg JP, and Leben RR. 1999. Coupled ocean-atmosphere dynamics in the Indian Ocean during 1997-98. *Nature* **401**: 356-360.
- Wilks, DS. 1995. *Statistical Methods in the Atmospheric Sciences: An Introduction*. Academic Press, 467pp.
- Xie, P, and Arkin PA. 1997. Global precipitation: A 17-year monthly analysis based on gauge observations, satellite estimates, and numerical model outputs. *Bull. Amer. Meteor. Soc.* **78**: 2539 - 2558.
- Xie, SP, Annamalai H, Schott, F and McCreary JP. 2002. Structure and mechanisms of south Indian Ocean climate variability. *J. Climate* **15**: 864-878.
- Zhang, C, Dong M, Gualdi S, Hendon HH, Maloney ED, Marshall A, Sperber KR, and Wang W. 2006. Simulations of the Madden-Julian Oscillation in four pairs of coupled and uncoupled global models. *Clim. Dyn.* **27**: 573-592.
- Zhong, A, Hendon HH, and Alves O. 2005. Indian Ocean variability and its association with ENSO in a global coupled model. *J. Climate* **18**: 3634-3649.

Table 1. Spatial correlation between Indian Ocean SST EOF1 from model forecasts at each lead time and SST EOF1 from observations for the SON season.

Lt1	Lt2	Lt3	Lt4	Lt5	Lt6	Lt7	Lt8	Lt9
0.91	0.83	0.70	0.62	0.55	0.56	0.55	0.56	0.58

Table 2. Temporal correlations between SST PC1 and the Niño3.4 index from model forecasts at each lead time and from observation (last column) for SON season.

Lt1	Lt2	Lt3	Lt4	Lt5	Lt6	Lt7	Lt8	Lt9	Obs
0.62	0.65	0.73	0.83	0.88	0.86	0.79	0.72	0.68	0.68

Figure Captions

- Figure 1.** Annual mean climatologies and monthly standard deviations in the equatorial Indian Ocean (2°S-2°N) for the period of 1982-2006 for a) and d) SST, b) and e) surface zonal wind and c) and d) depth of the 20 °C isotherm. Observations are solid line, and forecasts at lead time 1-, 3-, 6-, and 9-month lead times are open circles, closed squares, open diamonds, and pluses, respectively. Results from the AMIP run are included in b) and e) as thick dot-dash curve.
- Figure 2.** Seasonal cycle of the standard deviation of anomalies of a) the DMI and b) the Niño3.4 index. Observations are solid curves and hindcasts at 1-, 3-, 6-, and 9-month lead times are open circles, close squares, open diamonds, and pluses, respectively.
- Figure 3.** a) Standard deviation of SST (contour interval 0.1 °C) and EOF mode 1 (shaded; interval 0.05 °C) and (b) its principal component (standardized units) from observations in the SON season 1982-2006 for the Indian Ocean basin. EOF1 from ensemble mean of hindcasts at lead times 1-, 3-, 6-, and 9-months are shown in c)-f). The EOFs have been scaled for a one standard deviation anomaly of the respective principal components.
- Figure 4.** Regression of SST (left panel), and HC anomalies (right panel) onto principal component of EOF1 for SST in the Indian Ocean in SON. (a) and (f) are for observation; (b)-(j) are for ensemble mean of hindcasts at 1-, 3-, 6-, and 9-month lead times. Anomalies are scaled for a one standard deviation anomaly of the principal component. Contour interval for SST is 0.025 °C, and for HC is 0.04 °C (negative values are dashed). Zero contours are suppressed. Light (dark) shading denotes positive (negative) regression coefficients that are significant at the 95% level.
- Figure 5.** Same as Figure 4, but for precipitation (contours, interval 0.2 mm day⁻¹) and surface wind (vectors; scale in ms⁻¹ lower right). (a) is for observations; (b)-(e) are for ensemble mean hindcast at 1-, 3-, 6-, and 9-month lead times, respectively. Light (dark) shading denotes positive (negative) regression coefficients for precipitation that are significant at the 95% level. Wind vectors are plotted when either the u or v component is larger than ±0.04 m s⁻¹.
- Figure 6.** Temporal anomaly correlation coefficient between observed and ensemble mean SST at 1-, 3-, 6-, and 9-month lead times, respectively. Contour interval is 0.1 with correlations greater than 0.4 shaded (significant at the 95% level).

Figure 7. Temporal anomaly correlation coefficient (left panels) and normalized root mean square errors (NRMSEs, right panel) as a function of lead time for hindcasts (solid curves) and persistence (dot-dash curves) for DMI (a and e), EIO (b and f), WIO (c and g) and Niño3.4 (d and h). Also included in (e)-(h) is the standard deviation of the indices normalized by the observed standard deviation (NSTD, dashed curve).

Figure 8. Temporal anomaly correlation coefficient as a function of start month and lead time from hindcasts (left) and persistence (right) for (a) and (e) the Dipole Mode Index (DMI); (b) and (f) SST anomalies in the eastern pole (EIO: 90°-110°E, 10°S-0°); (c) and (g) SST anomalies in the western pole (WIO, 50°-70°E, 10°S-10°N); and (d) and (h) Niño 3.4 SST anomalies (170°-120°W, 5°S-5°N). Contour interval is 0.1 with negative values dashed. Regions with values above 0.6 are shaded. Faint sloping lines are for times of constant verification month.

Figure 9. As in Fig. 8 except for ratio of the variance of ensemble mean to total variance of ensemble (potentially predictable component of total variance; see text). Contour interval is 0.05 (dashed curves) for values less than 0.9 and 0.01 (solid curves) for values 0.9 and greater.

Figure 10. Hindcast predictions of monthly (a) DMI; (b) EIO; (c) WIO; and (d) Niño3.4 SST anomalies for 1994 (left panels), 1997(middle panels) and 2006 (right panels). Nine-month ensemble-mean hindcasts are displayed for initializations on 1 January (grey), 1 May (orange), 1 July (purple), 1 September (green), and 1 November (dark yellow). Thick black curve is verification.

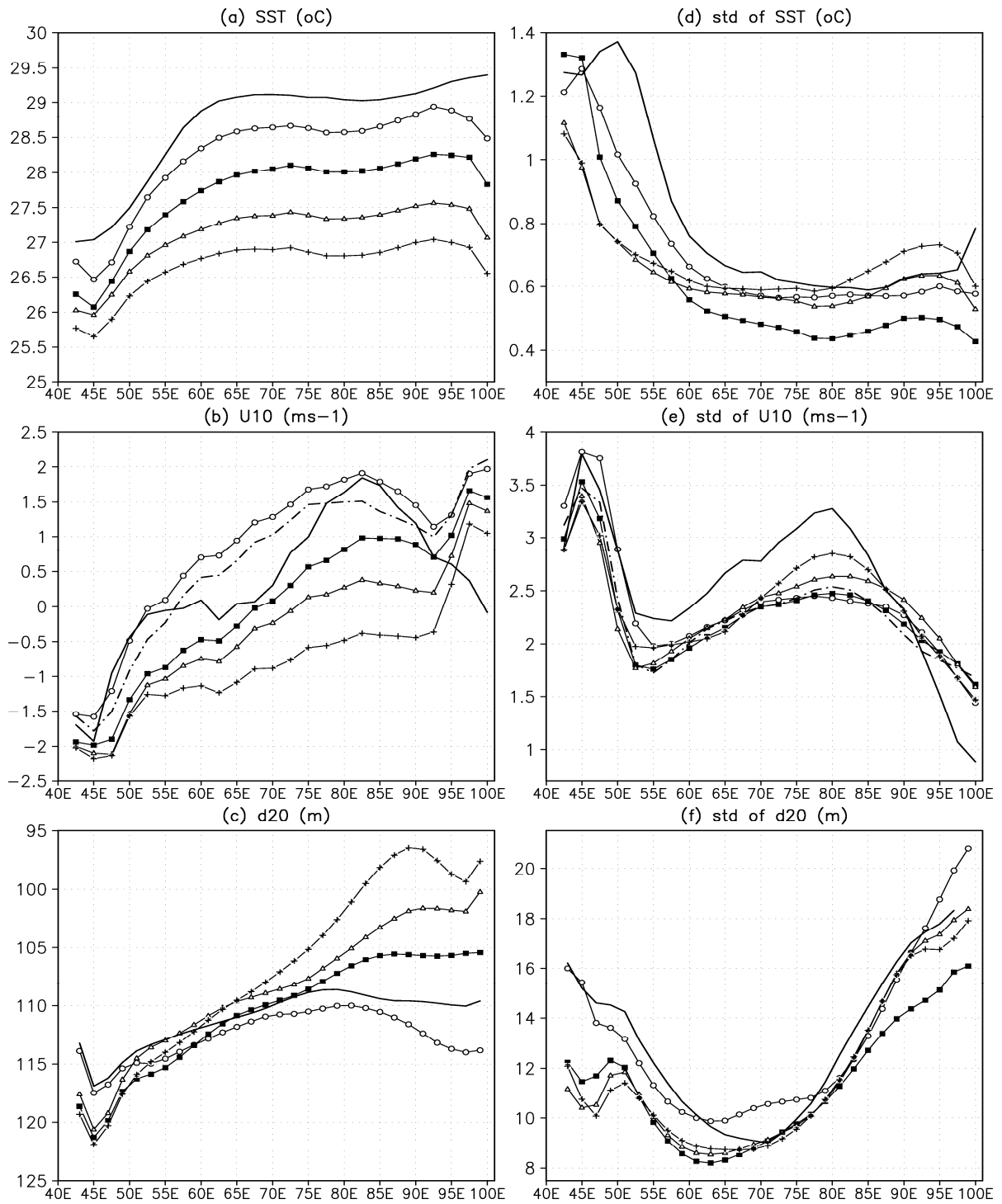


Figure 1. Annual mean climatologies and monthly standard deviations in the equatorial Indian Ocean (2°S-2°N) for the period of 1982-2006 for a) and d) SST, b) and e) surface zonal wind and c) and f) depth of the 20 °C isotherm. Observations are solid line, and forecasts at lead time 1-, 3-, 6-, and 9-month lead times are open circles, closed squares, open diamonds, and pluses, respectively. Results from the AMIP run are included in b) and e) as thick dot-dash curve.

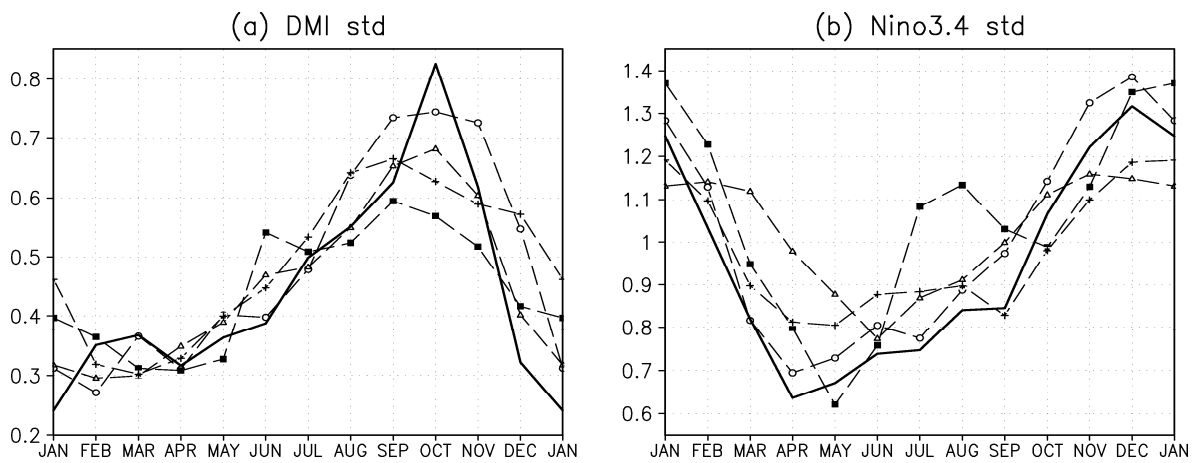


Figure 2. Seasonal cycle of the standard deviation of anomalies of a) the DMI and b) the Niño3.4 index. Observations are solid curves and hindcasts at 1-, 3-, 6-, and 9-month lead times are open circles, close squares, open diamonds, and pluses, respectively.

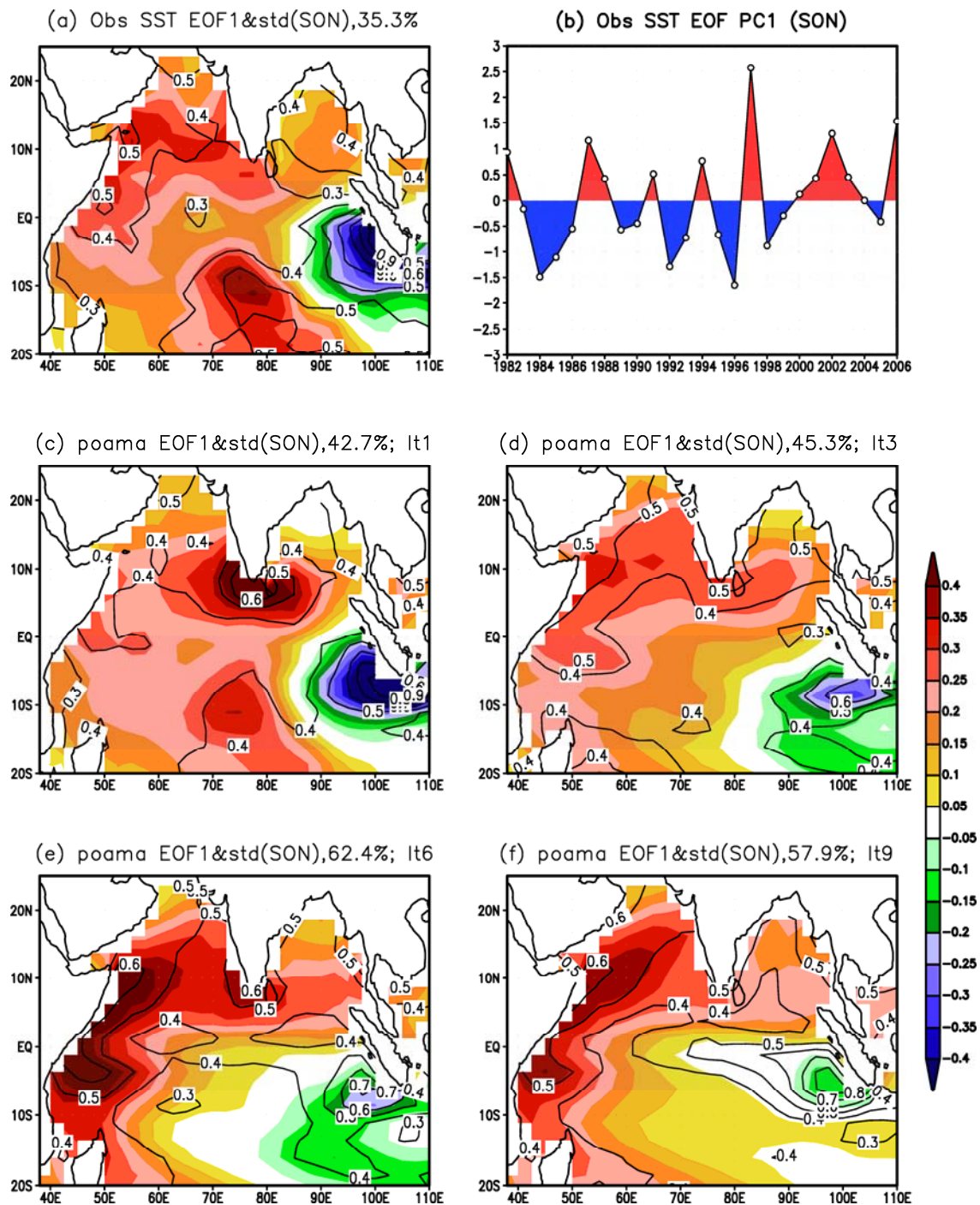


Figure 3. a) Standard deviation of SST (contour interval 0.1 °C) and EOF mode 1 (shaded; interval 0.05 °C) and (b) its principal component (standardized units) from observations in the SON season 1982-2006 for the Indian Ocean basin. EOF1 from ensemble mean of hindcasts at lead times 1-, 3-, 6-, and 9-months are shown in c)-f). The EOFs have been scaled for a one standard deviation anomaly of the respective principal components.

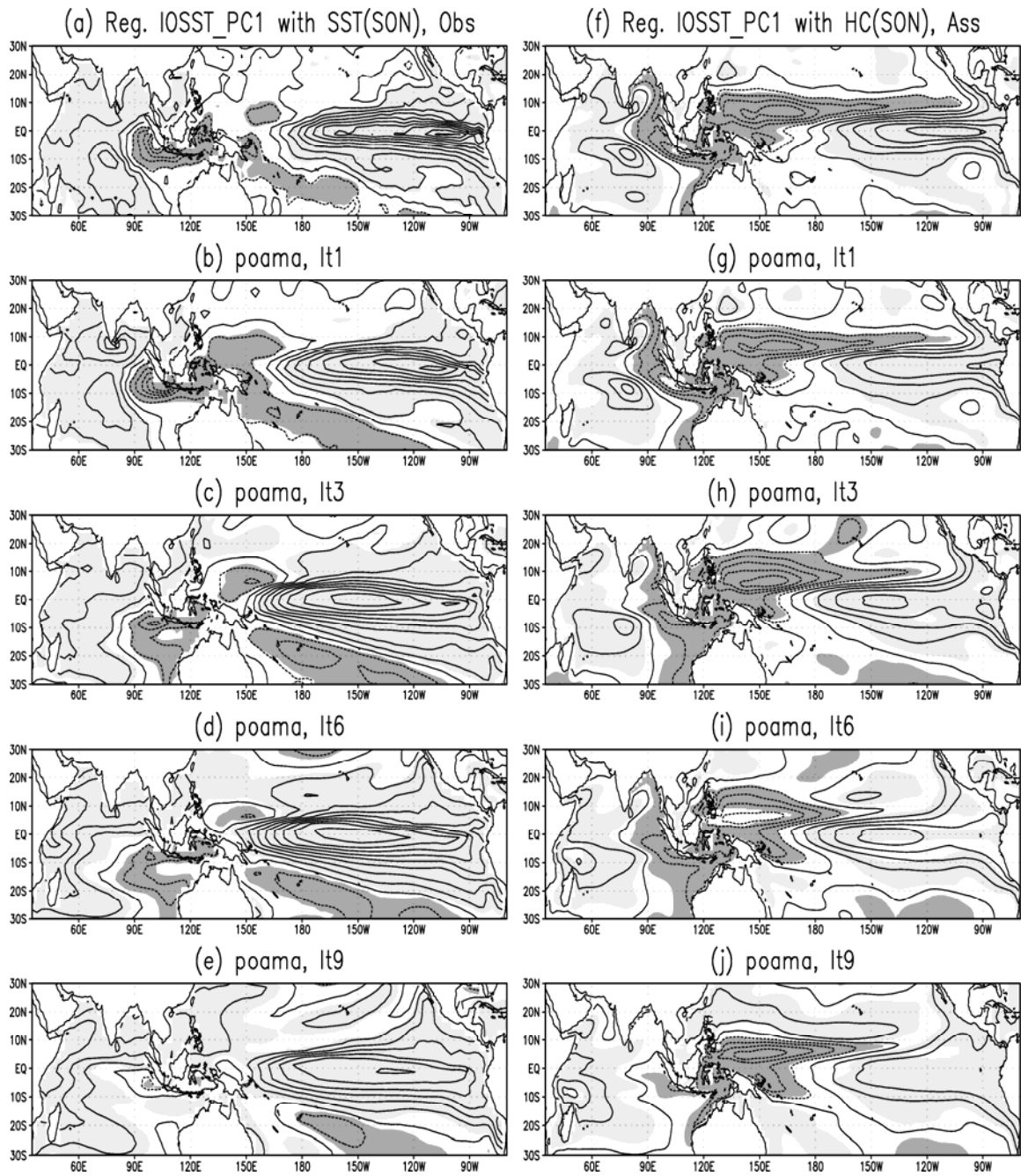


Figure 4. Regression of SST (left panel), and HC anomalies (right panel) onto principal component of EOF1 for SST in the Indian Ocean in SON. (a) and (f) are for observation; (b)-(j) are for ensemble mean of hindcasts at 1-, 3-, 6-, and 9-month lead times. Anomalies are scaled for a one standard deviation anomaly of the principal component. Contour interval for SST is $0.025\text{ }^{\circ}\text{C}$, and for HC is $0.04\text{ }^{\circ}\text{C}$ (negative values are dashed). Zero contours are suppressed. Light (dark) shading denotes positive (negative) regression coefficients that are significant at the 95% level.

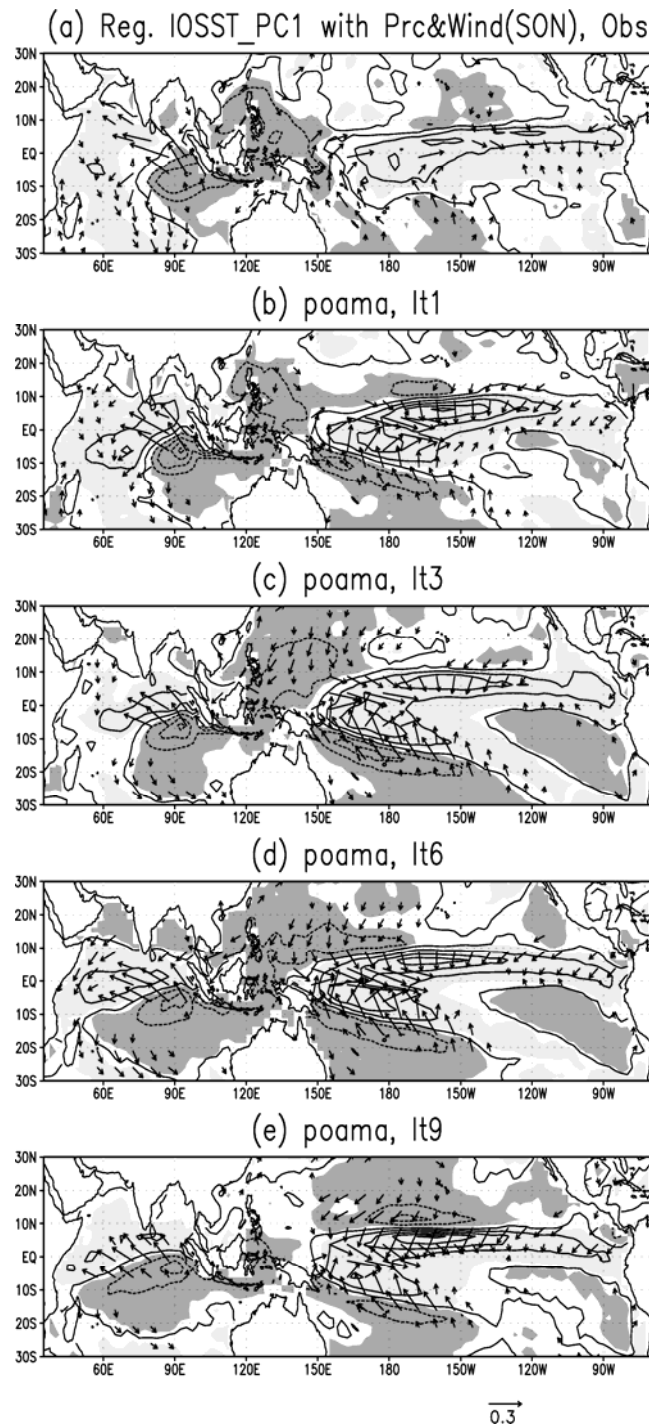


Figure 5. Same as Figure 4, but for precipitation (contours, interval 0.2 mm day^{-1}) and surface wind (vectors; scale in ms^{-1} lower right). (a) is for observations; (b)-(e) are for ensemble mean hindcast at 1-, 3-, 6-, and 9-month lead times, respectively. Light (dark) shading denotes positive (negative) regression coefficients for precipitation that are significant at the 95% level. Wind vectors are plotted when either the u or v component is larger than $\pm 0.04 \text{ m s}^{-1}$.

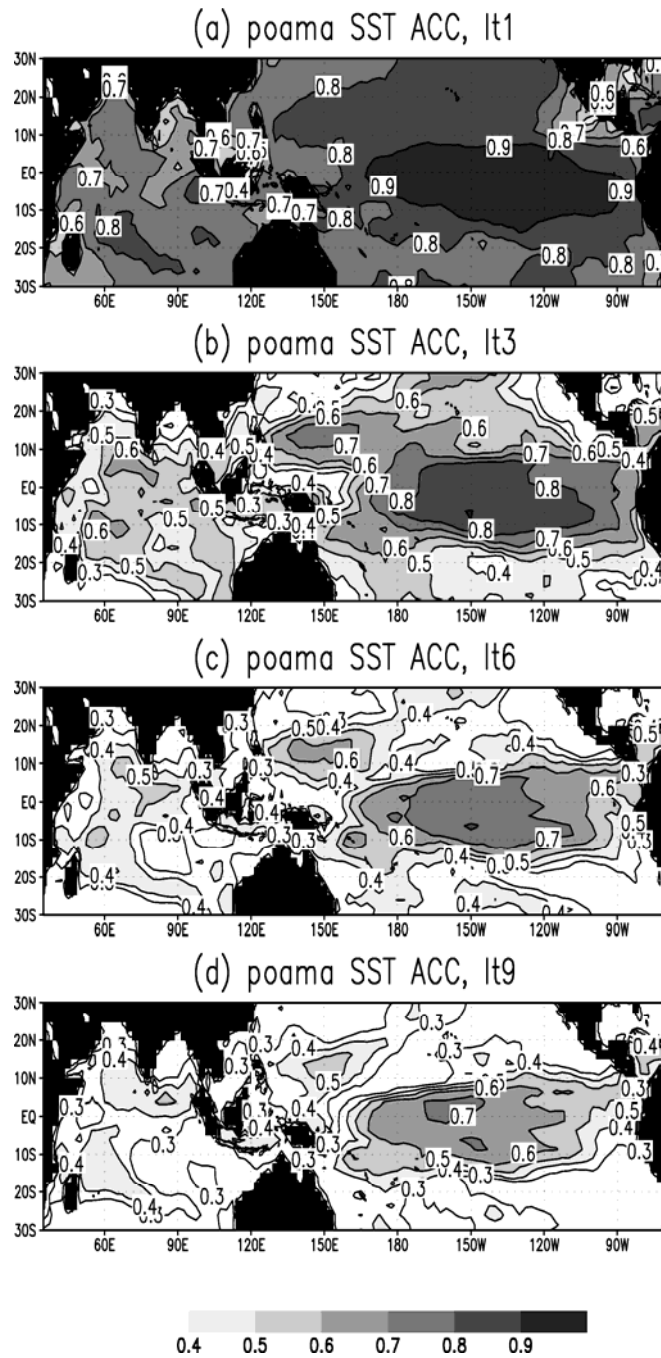


Figure 6. Temporal anomaly correlation coefficient between observed and ensemble mean SST at 1-, 3-, 6-, and 9-month lead times, respectively. Contour interval is 0.1 with correlations greater than 0.4 shaded (significant at the 95% level).

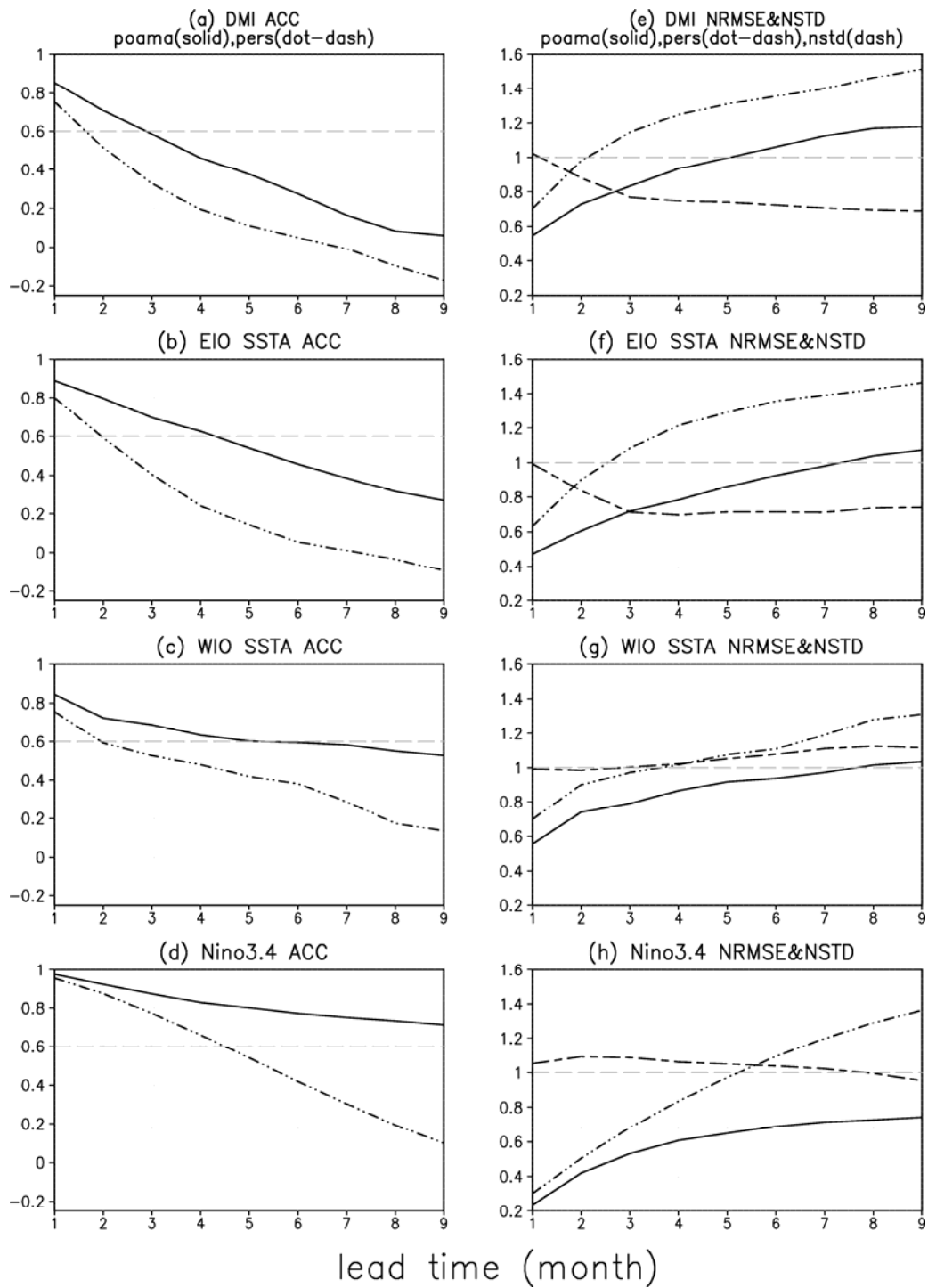


Figure 7. Temporal anomaly correlation coefficient (left panels) and normalized root mean square errors (NRMSEs, right panel) as a function of lead time for hindcasts (solid curves) and persistence (dot-dash curves) for DMI (a and e), EIO (b and f), WIO (c and g) and Niño3.4 (d and h). Also included in (e)-(h) is the standard deviation of the indices normalized by the observed standard deviation (NSTD, dashed curve).

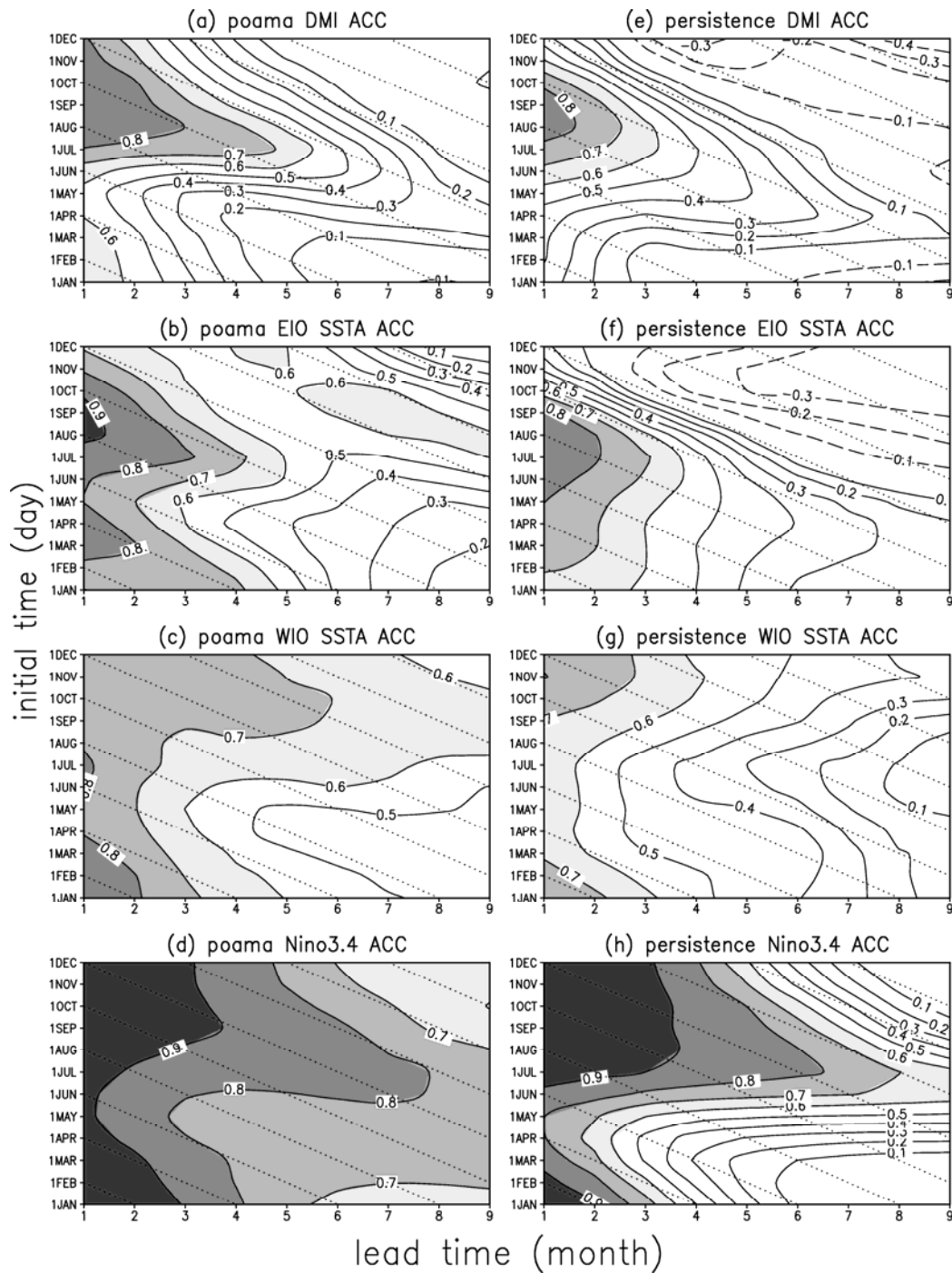


Figure 8. Temporal anomaly correlation coefficient as a function of start month and lead time from hindcasts (left) and persistence (right) for (a) and (e) the Dipole Mode Index (DMI); (b) and (f) SST anomalies in the eastern pole (EIO: 90°-110°E, 10°S-0°); (c) and (g) SST anomalies in the western pole (WIO, 50°-70°E, 10°S-10°N); and (d) and (h) Niño 3.4 SST anomalies (170°-120°W, 5°S-5°N). Contour interval is 0.1 with negative values dashed. Regions with values above 0.6 are shaded. Faint sloping lines are for times of constant verification month.

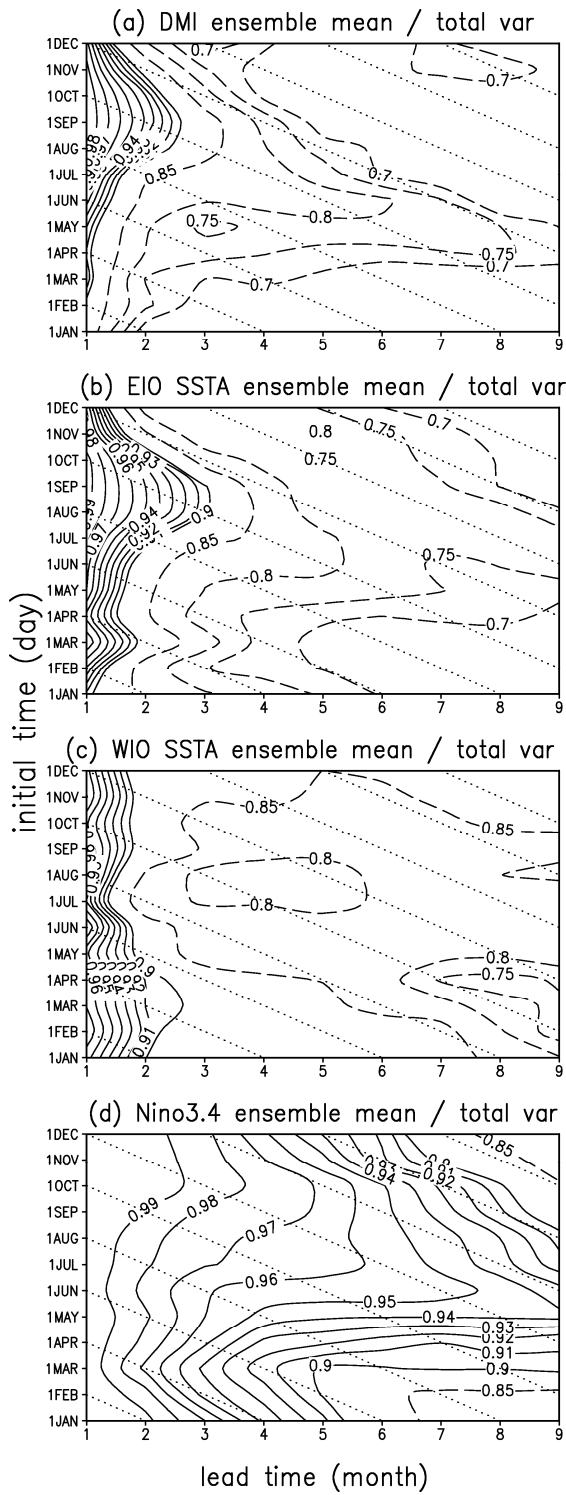


Figure 9. As in Fig. 8 except for ratio of the variance of ensemble mean to total variance of ensemble (potentially predictable component of total variance; see text). Contour interval is 0.05 (dashed curves) for values less than 0.9 and 0.01 (solid curves) for values 0.9 and greater.

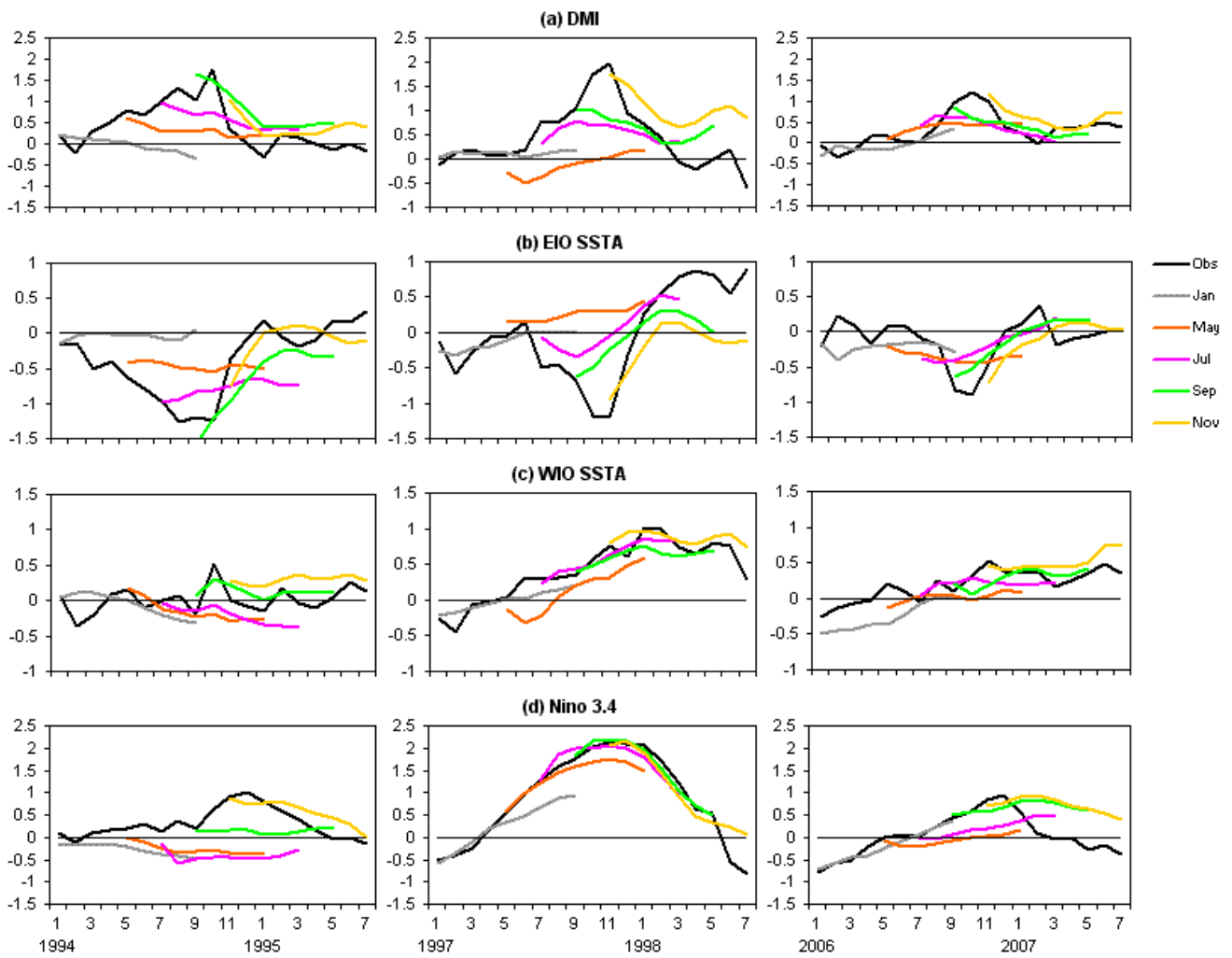


Figure 10. Hindcast predictions of monthly (a) DMI; (b) EIO; (c) WIO; and (d) Niño3.4 SST anomalies for 1994 (left panels), 1997(middle panels) and 2006 (right panels). Nine-month ensemble-mean hindcasts are displayed for initializations on 1 January (grey), 1 May (orange), 1 July (purple), 1 September (green), and 1 November (dark yellow). Thick black curve is verification.